Angular Spectrum Decomposition Analysis of Second Harmonic Ultrasound Propagation and its Relation to Tissue Harmonic Imaging

Xiang Yan and Mark F. Hamilton
Department of Mechanical Engineering,
The University of Texas at Austin, Austin, Texas 78712-1063

ABSTRACT

An angular spectrum decomposition method (ASM) for calculating second-harmonic propagation in fluid-like media is discussed. This method is based on a perturbation solution of Westervelt's equation, which can be augmented to take into account inhomogeneity of the medium. ASM can be applied to the analysis of tissue harmonic imaging (THI), a diagnostic method that utilizes second harmonics for imaging. One of the advantages of THI is the second harmonic's ability to improve image quality by reducing aberration caused by inhomogeneity in the body wall. The body wall aberration can be modeled as a localized phase screen in the wave propagation path. The results show that the interactions of angular spectrum components of the fundamental field generate a second-harmonic field that is relatively immune to the aberration. An experiment was performed to demonstrate this phenomenon by using a phase screen created from low density Polyethylene material. The measurements were in close agreement with calculations using ASM.

I. INTRODUCTION

When ultrasound propagates in fluid-like medium, due to nonlinearity inherent in the equations of motion and state, the waveform distorts progressively and new frequency components are generated. These nonlinear phenomena magnify as the amplitude of the ultrasound wave increases. The mechanism of nonlinear generation has been widely investigated and numerous model equations have been proposed under different conditions [1]. Westervelt's equation is chosen for our analysis for its inclusion of three dimensional diffraction, nonlinearity and absorption [1]. The solution of the Westervelt equation is solved under quasilinear conditions, in which the second-harmonic field level is one order smaller than the field level at the source frequency. When the ultrasound is transmitted at a single frequency *f*, the Westervelt equation can be written in the frequency domain, where the fundamental component propagates according to a homogeneous Helmholtz equation, and the second harmonic propagates according to an inhomogeneous Helmholtz equation with its forcing function determined by the fundamental field. These two equations can be solved separately by using a 2D spatial Fourier transform in the plane perpendicular to the propagation axis. This transform is called the angular spectrum of the wave field. The angular spectrum decomposition method (ASM) was first introduced in nonlinear acoustics by Alais and Hennion to analyze sum- and difference frequency generation by a nonlinear parametric array [2]. Subsequently it has been used to analyze reflection and refraction of the second-harmonic beam at a fluid-solid boundary [3]. In this paper, the method is used to analyze second-harmonic propagation when inhomogeneity is present in the medium.

A recent and very successful application of nonlinear acoustics is use of the second harmonics in diagnostic ultrasound, a modality frequently referred to as tissue harmonic imaging (THI). In

THI, the source transmits an ultrasound pulse at frequency *f*, and the receiver registers the signal at 2*f*. Although the second-harmonic amplitude is usually an order of magnitude smaller than that of the fundamental component, it is sufficiently high to be measured under conditions encountered in clinical cases [4, 5, 6]. Advances in ultrasound source design, detection instruments, and signal processing capability enable THI to be feasible.

THI is capable of improving image resolution due to its narrow main lobe and reduced side lobe reverberations [5,6,8,9]. A rule of thumb is that the main lobe directivity of the $2f$ beam can be approximated as the square of the main lobe directivity of the f beam. Second harmonics are also capable of reducing artifacts and haze due to their relative immunity to phase aberrations coming from intervening tissue inhomogeneity [5,8]. In conventional imaging (linear acoustics), the inhomogeneity introduces phase aberration in the f beam, which degrades the main lobe directivity and increases the side-lobe levels. But the self-interaction of the f beam, from which the second-harmonic ($2f$) is generated, is capable of filtering out these aberrations [5]. The generation of the second harmonic is strongest in regions where the fundamental field is strongest. The low side-lobe amplitudes are not sufficient to generate a second harmonic very efficiently, and therefore side lobe suppression is usually higher for the second harmonic beam than in the fundamental beam. Many numerical and experimental investigations have been conducted to assess quantitatively the nonlinear beam quality with aberrations in the medium, corresponding either to real inhomogeneous tissues [6,8] or constructed from tissue phantoms. [9,10,11]

In the present paper, we analyze second-harmonic generation and propagation using ASM taking into account inhomogeneity (phase aberrations) between the source and receiver. Measurements and simulations are focused on the distorted beam patterns introduced by the phase aberration. The aberration screen was constructed to provide phase variations having random distributions over the plane perpendicular to the propagation axis. The phase screen possesses statistics that are similar to those provided by Hinkleman based on measurements of human abdominal wall [12]. The simulated beam patterns obtained through ASM are compared with measurements. Finally, a quantitative measure called focusing quality, originally proposed by Tabei [13], is used to characterize the fundamental and second harmonic beam patterns.

II. Angular Spectrum Decomposition Method

In THI, the transmitted ultrasound is a short pulse instead of a single frequency. The frequency of the pulse is tuned properly to cover sufficient bandwidth in order to provide good axial resolution. On the other hand, the bandwidth should be sufficiently narrow to avoid overlapping of the fundamental and second-harmonic spectra [5]. To compare beam pattern distortion at two discrete frequencies *f* and 2*f*, a frequency domain analysis is efficient. Here we will assume that the source transmits a single frequency *f*, which greatly simplifies solution of the Westervelt equation.

The Westervelt equation, which describes the nonlinear propagation of ultrasound waves in an absorbing medium, is written as [1]

$$\nabla^2 p - \frac{1}{c_0^2}\frac{\partial^2 p}{\partial t^2} + \frac{\delta}{c_0^4}\frac{\partial^3 p}{\partial t^3} = -\frac{\beta}{\rho_0 c_0^4}\frac{\partial^2 p^2}{\partial t^2}, \quad \textbf{(1)}$$

where $\nabla^2 = \partial^2/\partial x^2 + \partial^2/\partial y^2 + \partial^2/\partial z^2$ and $p, \rho_0, c_0, \delta, \beta$ represent acoustic pressure, medium density, sound speed, sound diffusivity, and coefficient of nonlinearity, respectively. The right-hand side of Eqn. (1) accounts for the harmonic generation and is considered to be a small correction to the linear wave equation. We let $p = p_1 + p_2$, where $|p_1| >> |p_2|$, p_1 is the sound pressure at the fundamental frequency *f*, and p_2 is the sound pressure for the second harmonic, at frequency 2*f*. The higher harmonics are neglected due to their much smaller amplitudes and higher attenuations. Equation (1) is expanded according to the smallness of p_1 and p_2, and they are, individually, described by Helmholtz equations. Introducing the following notation,

$$p_n(\mathbf{r}, z, t) = \frac{1}{2j} P_n(\mathbf{r}, z) e^{jn\omega t} + \text{c.c.}, \quad \text{n} = 1,2. \quad \omega = 2\pi f \quad \textbf{(2)}$$

where $\mathbf{r} = (x, y)$, we arrive two equations describing the complex pressure $P_n(\mathbf{r}, z)$:

$$\nabla^2 P_1 + k_1^2 P_1 = 0, \quad \textbf{(3)}$$

$$\nabla^2 P_2 + k_2^2 P_2 = -\frac{j2\beta k^2}{\rho_0 c_0^2} P_1^2, \quad \textbf{(4)}$$

where $k_1^2 = k^2 - j\delta k^3/c_0$, $k_2^2 = 4k^2 - j8\delta k^3/c_0$, and $k = \omega/c_0$. Equations (3) and (4) are solved using ASM. The following 2D spatial Fourier transform pair is introduced:

$$\hat{P}(\boldsymbol{\kappa}, z) = F\{P(\mathbf{r}, z)\} = \int P(\mathbf{r}, z) e^{j\boldsymbol{\kappa}\bullet\mathbf{r}} d\mathbf{r}, \quad \textbf{(5)}$$

$$P(\mathbf{r}, z) = F^{-1}\{\hat{P}(\boldsymbol{\kappa}, z)\} = \int \hat{P}(\boldsymbol{\kappa}, z) e^{-j\boldsymbol{\kappa}\bullet\mathbf{r}} \frac{d\boldsymbol{\kappa}}{(2\pi)^2}, \quad \textbf{(6)}$$

where $\boldsymbol{\kappa} = (k_x, k_y)$ is wave number vector, see Figure 1. The Fourier transform pair shows that any pressure field $P(\mathbf{r}, z)$ can be viewed as a superposition of planes waves that propagate at angles determined by $\boldsymbol{\kappa}$. The amplitude of each plane wave is determined by the angular spectrum $\hat{P}(\boldsymbol{\kappa}, z)$. Talking the Fourier transforms of Eqns. (3) and (4), we arrive at the solution for P_1:

$$P_1(\mathbf{r}, z) = F^{-1}\{\hat{P}_1(\boldsymbol{\kappa}, z_0) e^{-jk_{z1}(z - z_0)}\}, \quad \textbf{(7)}$$

with

$$k_{z1} = \sqrt{k_1^2 - |\boldsymbol{\kappa}|^2} = \sqrt{k^2 - |\boldsymbol{\kappa}|^2 - j\delta k^3/c_0}, \quad \textbf{(8)}$$

where $\hat{P}_1(\boldsymbol{\kappa}, z_0)$ is the known angular spectrum distribution at a given propagation distance z_0, and z is at the target plane, with $z > z_0$. The solution for P_2 is composed of two parts, P_2^h, which accounts for linear propagation of $P_2(\mathbf{r}, z_0)$ from z_0 to z, and P_2^p, which is the nonlinear generation from $P_1(\mathbf{r}, z)$ from z_0 to z. The first part, P_2^h, has a form similar to Eq. (7), and is obtained by changing k to $2k$. The solution for P_2^p comes from the nonlinear interactions of plane waves represented by $\hat{P}_1(\boldsymbol{\kappa}, z_0)$, which is found to be [3,15]

$$P_2^p(\mathbf{r}, z) = F^{-1}\left\{\hat{P}_2^p(\boldsymbol{\kappa}, z) e^{-jk_{z2}(z-z_0)}\right\}, \tag{9}$$

$$\hat{P}_2^p(\boldsymbol{\kappa}, z) = \frac{j\beta k^2}{2\pi^2 \rho_0 c_0^2} \int \frac{\hat{P}_1(\boldsymbol{\kappa}', z_0)\hat{P}_1(\boldsymbol{\kappa} - \boldsymbol{\kappa}', z_0)}{(k_a + k_b)^2 - k_{z2}^2} \left[e^{-j(k_a + k_b - k_{z2})(z-z_0)} - 1\right] d\boldsymbol{\kappa}', \tag{10}$$

with

$$k_a = \sqrt{k^2 - |\boldsymbol{\kappa}'|^2 - j\delta k^3 / c_0}, \quad k_b = \sqrt{k^2 - |\boldsymbol{\kappa} - \boldsymbol{\kappa}'|^2 - j\delta k^3 / c_0}, \tag{11}$$

and

$$k_{z2} = \sqrt{4k^2 - |\boldsymbol{\kappa}|^2 - j8\delta k^3 / c_0}. \tag{12}$$

The total solution of $P_2(\mathbf{r}, z)$ is the sum of $P_2^h(\mathbf{r}, z)$ and $P_2^p(\mathbf{r}, z)$, i.e.,

$$P_2(\mathbf{r}, z) = F^{-1}\left\{\left(\hat{P}_2^h(\boldsymbol{\kappa}, z_0) + \hat{P}_2^p(\boldsymbol{\kappa}, z)\right) e^{-jk_{z2}(z-z_0)}\right\}. \tag{13}$$

From Eqns. (10) ~ (12) one can see that the angular spectrum for the second harmonic $\hat{P}_2(\boldsymbol{\kappa}, z)$ broadens due to the doubling of frequency and convolution-like filtering with $\hat{P}_1(\boldsymbol{\kappa}, z_0)$. A broader spectrum indicates a narrower beam width. Equations (12) and (13) also indicate that the second harmonic spectrum at distance *z* depends only on the fundamental spectrum at distance z_0, assuming the intervening medium is homogeneous. This facilitates the calculation of second harmonics since there are no intermediate calculations are needed. Although the second harmonic is generated cumulatively from z_0 to *z*, the perturbation assumption and frequency domain calculation eliminate any intermediate steps.

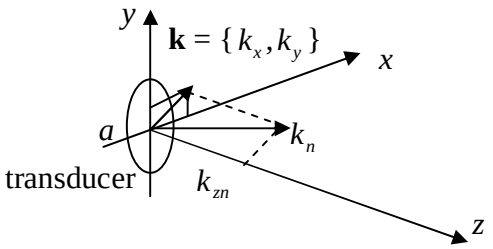

Figure 1 Geometry of ultrasound beam propagation, transducer is located in plane $z = 0$, propagation is along *z* axis.

It is also possible to include inhomogeneity along the propagation path, provided these regions are localized and lend themselves to modeling with phase screens. In THI, significant inhomogeneity comes from the scattering from septa in the subcutaneous fat in the body wall [16]. This localized aberration causes a phase change that can be modeled as phase screen [12], which makes ASM suitable for analyzing THI. Suppose the phase screen is situated at z_s and introduces a phase modulation to $P_n(\mathbf{r}, z_s)$. The ASM computation then separates into two parts. First, the pressures $P_n(\mathbf{r}, z)$ are calculated from $z = 0$ to $z = z_s$ using Eqs. (7) and (10), with $P_2^h(\mathbf{r},0) = 0$. Then, at z_s, phase aberrations are applied to $P_n(\mathbf{r}, z)$ and $P_n(\mathbf{r}, z)$, which then propagate from z_s to z individually. Notice that the phase change doubles for the second harmonic due to the wavelength being half that of the fundamental. If medium inhomogeneity is distributed along the propagation path, multiple phase screens can be applied and calculations can be done from screen to screen.

Early models for THI assume that the tissue is homogenous [6]. Later models taking inhomogeneity into account involved numerical simulations with nonlinear propagation algorithms that march the wave field forward incrementally step by step. Christopher [8] modeled the body wall inhomogeneity with phase screens and propagated the wave field incrementally thereafter. A time-domain algorithm for solving the KZK algorithm has also been used to model inhomogeneity with terms included that account for continuous variations of the sound speed and density [11]. All results show that even in the presence of aberrations, the second-harmonic field still provides better beam quality than the fundamental field. The second-harmonic field exhibits a tighter main lobe and lower side lobes than the fundamental beam.

III. MEASUREMENT

In this paper, the second-harmonic field is calculated using ASM with inhomogeneity taken into account by phase screens. Experiments were performed and compared with calculations. The experimental setup is shown in Figure 2. A focused circular piston source (Panametrics Acuscan series) with center frequency 2.25 MHz, diameter 38 mm and focal length 152 mm, was placed in a water tank in front of a phase screen that was created by machining a uniform 3 mm-thick low-density polyethylene plate to varying thickness over one of its surfaces. The focal beam patterns were measured using a PVDF membrane hydrophone. The hydrophone was used to scan over the plane perpendicular to the propagation axis. The source, hydrophone and plate were all immersed in a water tank containing de-ionized, degassed fresh water.

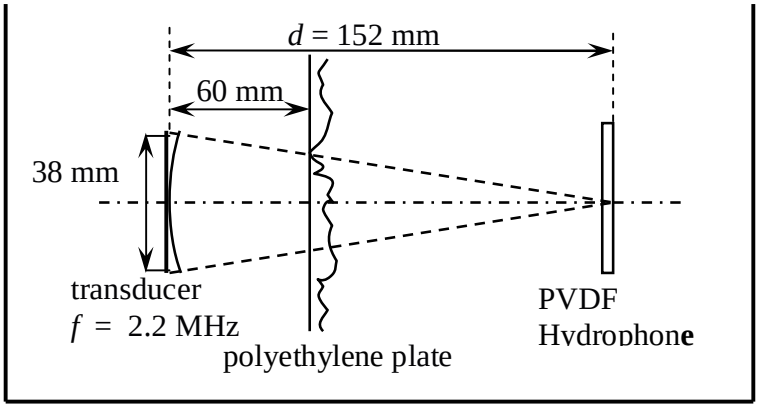

Figure 2. Experiment set-up. A phase screen made from low-density polyethylene plate is placed in front of a focused transmitter to simulate the aberration caused by body wall.

Random indentations were engraved on the plate to introduce phase aberration. They were small circular cuts that were randomly distributed on the surface according to a desired statistical distribution. All the circles had the same 1 mm indentation. This indentation introduced a 2.7 rad phase shift at 2.25 MHz. Two patterns were created with different circle diameters and different spatial distributions, as shown in Figure 3 . Screen A had 200 small circles with diameter of 3.18 mm distributed over an area of 100 mm x 100 mm. Screen B had 40 circles with diameter 12.7 mm distributed over the same area. Their inhomogeneity length scales are described by the characteristic lengths of the 2D autocorrelation functions (correlation lengths). This is the interval between the half maximum amplitude points of the autocorrelation function. Screen A had an inhomogeneity length scale of about 3 mm, and screen B of about 11.7 mm, which are close to the diameters of the circles. These two values correspond to the measured minimum and maximum inhomogeneity length scales of the human abdominal wall. [12]

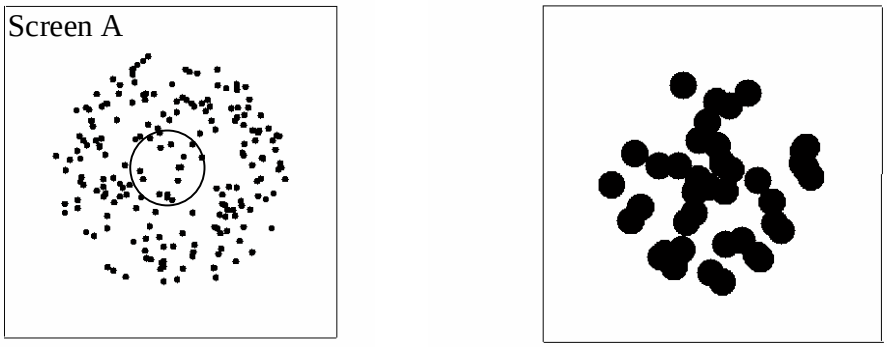

Figure 3. Geometry of circle indentations in the polyethylene plates used as the phase screens. The big circle indicates the size of the transmitter (38 mm diameter). The circles indicate the relative size of the circular source.

In addition to introducing phase changes, the phase screen also introduces amplitude aberrations due to the impedance mismatch and absorption. It is estimated that the amplitude variation across the phase screen is within 10%. This amplitude perturbation has a substantially smaller effect on the wave field than the phase changes, and it can be neglected without introducing significant error [15]. The insertion loss introduced by the plate can be compensated for by increasing the drive level. The finite thickness of the phase screen (maximum 3 mm) is about 3 wavelengths of the fundamental field. The refraction introduced by the plate can slightly reduce the focal distance, but in the case of a beam at normal incidence, the effect is found to be negligible. Under conditions of the experiment, the plate is was as a phase screen with zero thickness, introducing uniform amplitude variation and random phase in the calculations.

In the measurements, the transmitted signals are monofrequency pulses (around 15 cycles) at 2.25 MHz generated by a HP 3314A function generator. They were amplified by 50 dB before being sent to the transducer. The signal received by the hydrophone was amplified by 20 dB before digitization. The digitized waveform was finally sent to the computer to be analyzed. A time domain FFT was used to extract the spectrum information from the waveforms.

IV. RESULTS

The focal beam patterns for the fundamental and second harmonic fields were measured first without the phase screen. The results are shown in Figure 4. They are compared with the ASM calculation using Eqns. (7), (9) and (10), and it is seen that good agreement is achieved. The beam patterns exhibit good axial symmetry. The measured beam patterns do not show deep nulls as compared to the simulations due to the deviation of the source condition from an ideal piston and the finite frequency bandwidth of the CW pulse. The calculated angular spectra of the beam patterns are shown in Figure 5. The spatial frequencies are normalized to the wavelength, i.e., λf_x (at 2.25MHz), where $f_x = k_x / 2\pi$. Figure 5 shows that the angular spectrum of the fundamental (Fig. 5a) has isolated ring-type components, whereas that of the second harmonic (Fig. 5b) is more continuously distributed and spreads out over a larger domain, which explains the narrow main lobe for the second harmonics. Continuous spectral distributions of the second harmonics result from the convolution-like interactions of fundamental spectrum as shown in Eqn. (10), which acts like a smooth filter. The resulting pressure field, after applying the inverse FFT to the angular spectrum, possesses reduced side lobes.

For the case in which phase screen A is placed between the transmitter and receiver, as shown in Figure 2, the measured and simulated focal beam patterns are as shown in Figure 6. One sees readily that the scattered side lobe levels are greatly increased, while the main lobes are less affected. The ASM simulated beam patterns predict these results and agree well with the measurements. The angular spectra are shown in Figure 7. When comparing Figure 7(a) with Figure 5(a), one can see there is a significant amount of energy scattered to the higher angular frequencies. The frequency distribution has isolated patches, with a small amount of energy concentrated around the dc component, and a ring structure is observed at high spatial frequencies. The interference of the high frequency spectrum with the low frequency spectrum increases side lobe levels in the beam pattern, and this in turn leads to increased reverberation. The spectrum for the second harmonic, Figure 7(b), exhibits similar distortion, also leading to increased side lobe levels. But compared to Figure 7(a), the second harmonic spectrum is more

continuously distributed and the corresponding side lobe levels are obviously lower than fundamental beam.

The focal beam patterns resulting from use of screen B are shown in Figure 8, and their angular spectra are shown in Figure 9. Screen B has a larger inhomogeneity length scale that scatters less energy into the high spatial frequencies in comparison to screen A, and their spectra clearly illustrate this point. The second harmonic spectrum, Figure 9(b), almost maintains the same shape and continuity as in Figure 5(b).

The measured width of the main lobe (3-dB beam width) and maximum side lobe levels for fundamental and second harmonics are presented in Table 1.

	$\theta_{3\text{dB}}$ main lobe width		Maximum side lobe level	
	fundamental	2nd harmonic	fundamental	2nd harmonic
No screen	2.9 mm	1.7 mm	-17.6 dB	-26.2 dB
Screen A	2.8 mm	1.5 mm	-8.2 dB	-12.2 dB
Screen B	3.7 mm	2.0 mm	-10.0 dB	-15.0 dB

Table 1. 3-dB main lobe beam width and maximum side lobe levels for the measured fundamental and second harmonic beam patterns.

Another quantitative measure for a focused beam pattern, referred as the focusing quality, was proposed by Tabei [13] to characterize the degradation of the focus caused by aberration. The focusing quality is defined as the reciprocal of the Peripheral Energy Ratio (PER), i.e., the ratio of acoustic energy in the peripheral area to the energy in the focal area,

$$Q = \frac{E_{\text{foc}}}{E_{\text{peri}}}. \qquad \textbf{(14)}$$

The focal area is defined as the region where amplitude is within half of the peak value in the beam, and the peripheral area is the rest of the measurement area outside this focal area. The focusing quality Q for the measured beam patterns are shown in Table 2. One can see that Q is decreased in the presence of aberration. The value of Q for second harmonic beam is always larger than the value for the fundamental. The discrepancy in their values of Q is even larger in the case of the phase screen. This means that the phase screen causes more degradation of the fundamental field than of the second harmonic field.

	Focusing Quality Q	
	Fundamental	2nd harmonic
No screen	2.0	2.4
Screen A	0.7	1.3
Screen B	1.4	2.3

Table 2. Focusing quality Q for the measured fundamental and second harmonic beam patterns.

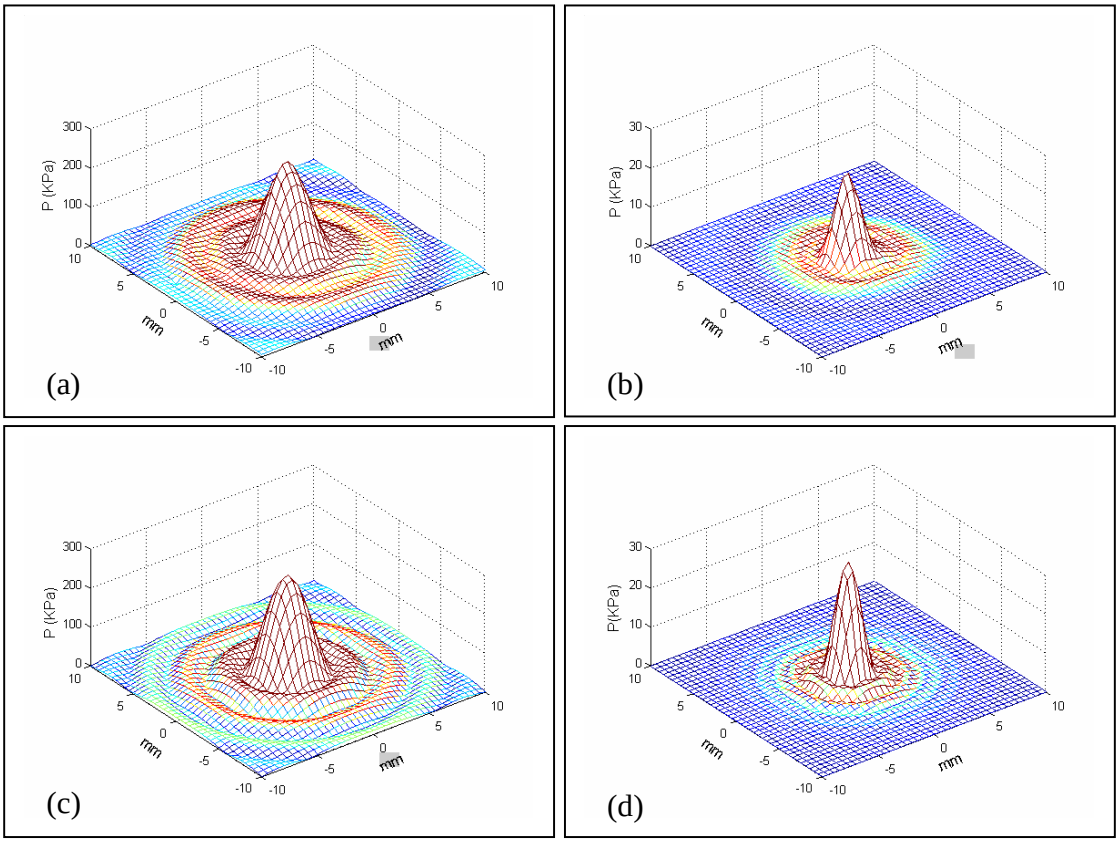

Figure 4. Measured fundamental (a) and second harmonic (b) beam patterns compared to calculated fundamental (c) and second harmonic (d) beam patterns using angular spectrum method in the absence of phase screen.

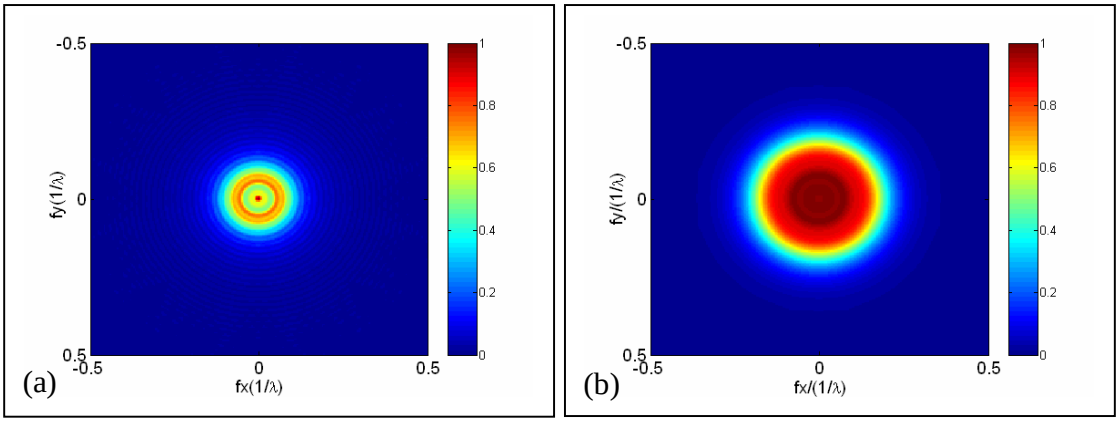

Figure 5. Calculated normalized angular spectrum distribution for fundamental (a) and second harmonic (b) beam pattern with no phase aberration.

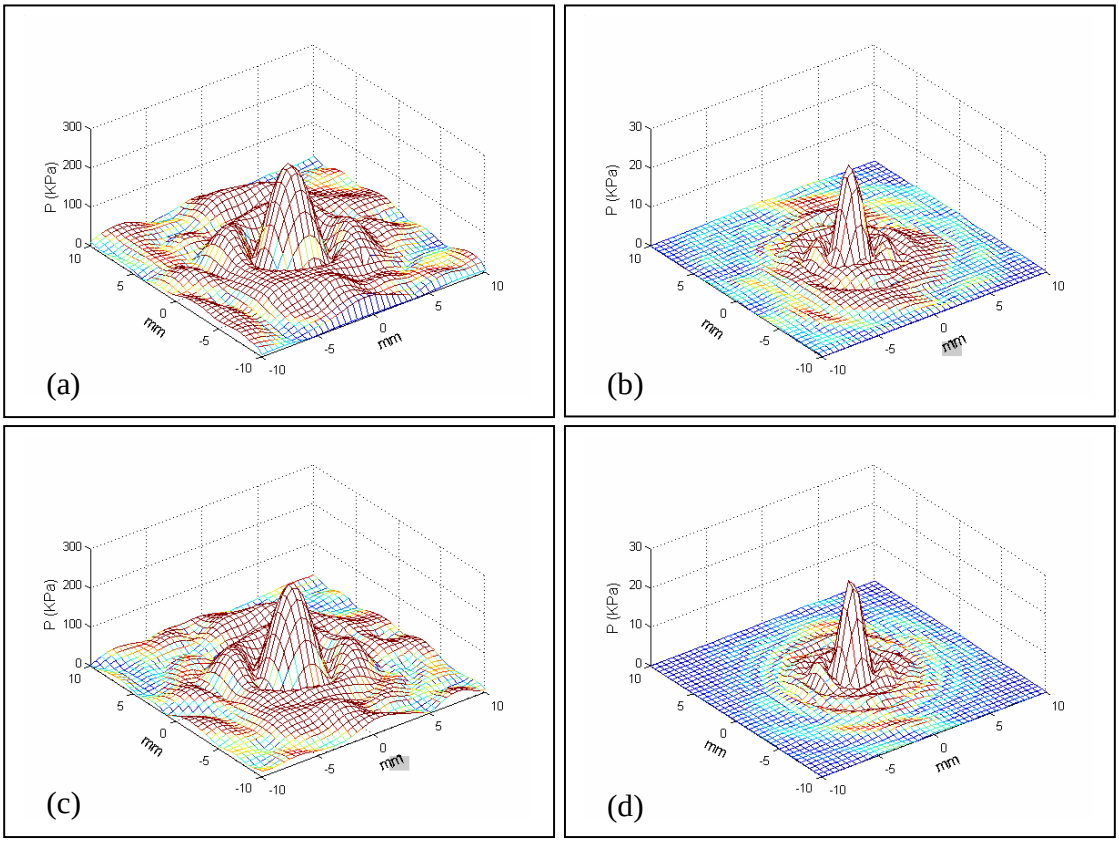

Figure 6. Measured fundamental (a) and second harmonic (b) beam patterns compared to calculated fundamental (c) and second harmonic (d) beam with phase screen A in the propagation path.

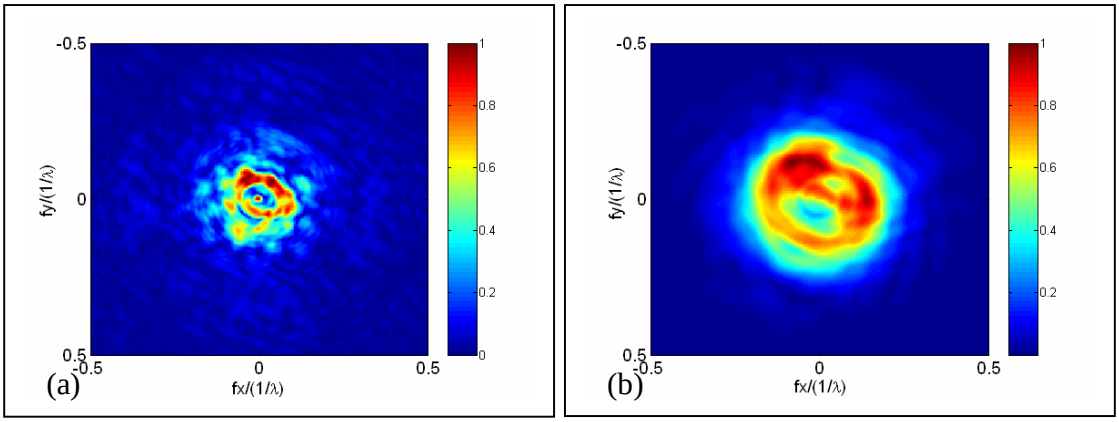

Figure 7. Calculated normalized angular spectrum distribution for fundamental (a) and second harmonic (b) beam pattern with phase screen A.

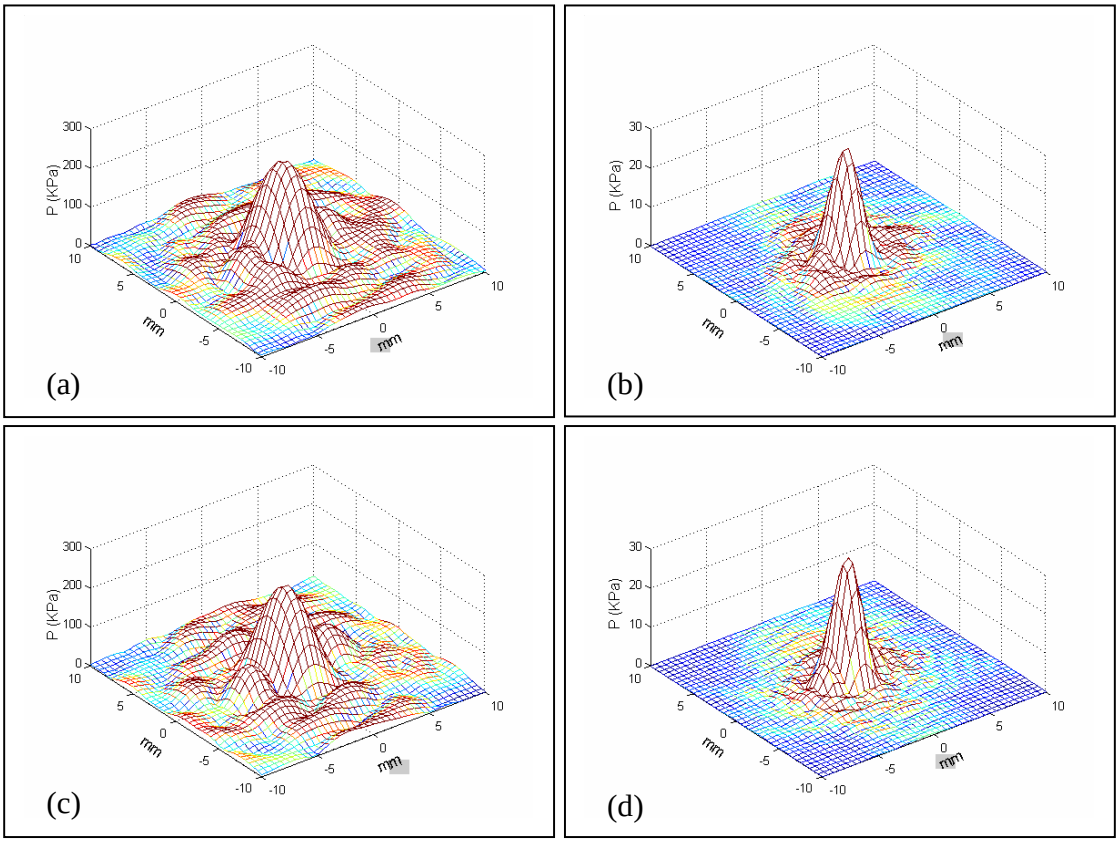

Figure 8. Measured fundamental (a) and second harmonic (c) beam patterns compared to calculated fundamental (b) and second harmonic (d) beam with phase screen B in the propagation path.

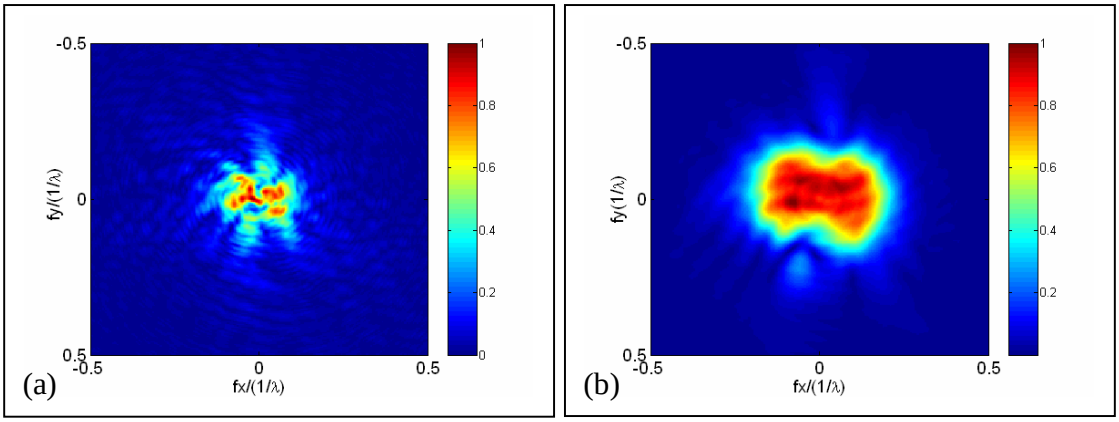

Figure 9. Calculated normalized angular spectrum distribution for fundamental (a) and second harmonic (b) beam pattern with phase screen B.

From the above discussion, one can see that second harmonic generation and propagation is inherently filtered in such a way that its angular spectrum is smoothed and maintains its continuity, even when components in spectrum of the fundamental are scattered into isolated bands (in the spatial frequency domain) due to inhomogeneity. The filtering process arises from the nonlinearity of the hydrodynamics and the state equations that characterize the pressure in the propagation medium as indicated by Eqn. (4) in space domain. The continuity of its angular spectrum ensures that the second harmonic side lobes are at a low level. At the same time, the width of the main lobe is reduced due to doubling of the frequency. The main difference between the nonlinearly generated second harmonic and the linear second harmonic is the side lobe level difference. The linear wave at the second harmonic (*2f*) has a narrower main lobe and more side lobes, and the inhomogeneity creates twice the phase variation at *2f*, which drives the side lobes to higher levels than in the fundamental beam (*f*) [15]. Therefore the enhanced scan resolution of the linear *2f* beam is at the cost of increased artifacts and haze. The nonlinear second harmonics thus provide enhanced scan resolution and reduced artifacts. The cost is the lower amplitude of the signal, and therefore lower signal-to-noise ratio, leading to the requirement of a more sensitive receiver and lower noise amplifier.

V. CONCLUSION

In this paper we investigate the angular spectrum of the second harmonic arising from the nonlinear propagation of an ultrasonic wave in fluid-like medium. The angular spectrum in the observation plane can be described as an integral over the angular spectrum of fundamental component in the source plane, provided the intervening medium is homogeneous. This method is adapted to account for inhomogeneity of the medium encountered during THI. The inhomogeneity arising from the body wall is modeled as a phase screen. Measurements and corresponding simulations have been presented for the scattered beam patterns radiated from a focused piston source through an artificial random phase-screen. The statistics of the phase screen correspond to the measured human abdominal wall statistics. The simulation employing ASM agrees well with the measurements, and the reduced side lobe reverberation of the second harmonics is explained from the angular spectrum point of view. The focusing quality factor quantifies the beam degradation and shows improvement of second harmonic beam over fundamental beam. This provides a theoretical basis to explain the reduced artifacts and haze in the image quality in THI.

REFERENCES

1. M. F. Hamilton, ``Model Equations," in *Nonlinear Acoustics*, edited by M. F. Hamilton and D. T. Blackstock (Academic Press, Boston, 1998), Chap.~3.
2. P. Alais and P. Y. Hennion, ``A Fourier theory of the nonlinear interaction of acoustical beams in absorbing fluid. The spectral case of parametric emission," Acustica 43, 1—11 (1979).
3. B. J. Landsberger and M. F. Hamilton, ``Second harmonic generation in sound beams reflected from, and transmitted through immersed elastic solid," *J. Acoust. Soc. Am* 109, 488--500 (2001).
4. M. A. Averkiou, ``Tissue harmonic imaging," *IEEE Ultrasonics Symposium*, **2**, 1563--1572 (2000).
5. M. A. Averkiou, ``Nonlinear acoustics in tissue harmonic imaging," J. *Acoust. Soc. Am.* 114, 2435 (2003).
6. M. A. Averkiou, D. N. Roundhill, and J. E. Powers, ``A new imaging technique based on the nonlinear properties of tissues," *IEEE Ultrasonics Symposium* 2, 1561—1566, (1997).
7. B. Ward, A. C. Baker and V. F. Humphrey, ``Nonlinear propagation applied to the improvement of resolution in diagnostic medical ultrasound," *J. Acoust. Soc. Am.* 101, 143--154 (1997).
8. P. T. Christopher, ``Finite amplitude distortion-based inhomogeneous pulse echo ultrasonic imaging," *IEEE Trans. Ultrason. Ferroelctr. Freq. Control* 44, 125--139 (1997).
9. G. Wojcik, J. Mould, S. Ayter, and L. Carcione, ``A study of second harmonic generation by focused medical transducer pulses," *IEEE Ultrasonics Symposium*, 1583--1588 (1998).
10. P. T. Christopher, ``Experimental investigation of finite amplitude distortion-based second harmonic pulse echo ultrasonic imaging," *IEEE Trans. Ultrason. Ferroelctr. Freq. Contro*} **45**, 158--162 (1998).
11. Y. Jing, X. Yang and R. Cleveland, ``Experimental and numerical investigation of tissue harmonic imaging (THI)," *J. Acoust. Soc. Am* 113, 2324 (2003).
12. L. M. Hinkelman, D.-L. Liu, L. A. Metlay, and R. C. Waag, ``Measurements of ultrasonic pulse arrival time and energy level variations produced by propagation through abdominal wall," *J. Acoust. Soc. Am.* 95, 530--541 (1994).
13. M. Tabei, T. D. Mast, and R. C. Waag, ``Simulation of ultrasonic focus aberration and correction through human tissue," *J. Acoust. Soc. Am.* 113, 1166—1176 (2003).
14. M. F. Hamilton, ``Sound Beams," in *Nonlinear Acoustics*, edited by M. F. Hamilton and D. T. Blackstock (Academic Press, Boston, 1998), Chap.~8.
15. X. Yan, ``Statistical model of beam distortion by tissue inhomogeneities in tissue harmonic imaging," Ph.D. dissertation, The University of Texas at Austin (2004).
16. T.D. Mast, L.M. Hinkelman, M. J. Orr, V. W. Sparrow and R. C. Waag, " Simulation of ultrasonic pulse propagation through the abdominal wall," J. Acoust. Soc. Am. **102**, 1177-1190 (1997).